

PTEN regulates actin filaments to shape cell cortex architecture

Kimberly Ho

New York University Long Island School of Medicine

Suraj S. Patel

Weill Cornell Medicine

Eve Sullivan

Weill Cornell Medicine

Alicia Chang

Columbia University

Guang Han Lin

Yale University

Moqi Lv

Xi'an Jiaotong University School of Medicine

Xinyi Fan

Weill Cornell Medicine

E. R. Naufal

Weill Cornell Medicine

Wen H. Shen (✉ wes2007@med.cornell.edu)

Weill Cornell Medicine

Article

Keywords: PTEN, actin polymerization, moesin, phosphorylation, subcellular localization

Posted Date: January 3rd, 2023

DOI: <https://doi.org/10.21203/rs.3.rs-2375922/v1>

License: © ⓘ This work is licensed under a Creative Commons Attribution 4.0 International License.

[Read Full License](#)

Abstract

Mitosis and homeostasis depend on proper cellular morphological transformation and plasma membrane structure during interphase. PTEN is a tumor suppressor protein involved in cellular homeostasis and genomic stability. We have previously shown that loss of PTEN leads to impairment of mitotic spindle architecture and cytokinesis. Here we report a potential relationship between PTEN and actin in controlling cellular morphology. *PTEN* depletion results in disorganization of the actin cytoskeleton. This is manifested by decreased parallel alignment of actin filaments, increased F-actin at the membrane, and cells appeared rounder. We also found that Moesin (Moe), an actin-binding ERM protein involved in membrane morphology, exhibits greater level in the phosphorylated Moe (pMoe) form and dislocation of pMoe from the cell cortex. Using an inhibitor of actin polymerization in PTEN-deficient cells, our data show a reduced quantity of pMoe and the recovery of its membrane enrichment. Moreover, inhibition of actin polymerization also reduces F-actin at the membrane and the frequency of cells with round shape. These data suggest that PTEN may regulate cortical actin polymerization to maintain cellular morphology and membrane dynamics.

Introduction

Phosphatase and tensin homologue deleted on chromosome 10 (*PTEN*) encodes a protein that negatively regulates the phosphoinositide 3-kinase (PI3K)/AKT signaling pathway for cell survival and proliferation.¹⁻³ In addition, it regulates cell metabolism^{4,5}, cell cycle progression^{6,7}, cell motility^{8,9}, stem cell self-renewal^{10,11}, the structural integrity of chromosomes^{12,13}, DNA replication¹⁴, repair¹⁵, decatenation¹⁶, mitosis¹⁷⁻¹⁹, and chromatin remodeling^{20,21}.

PTEN has been reported to control multicell morphological coordination by maintaining membrane localization of protein complexes²². It regulates mitotic cell shape transformation, cell elongation, and cytokinesis by recruitment of moesin (Moe), a crosslinker between the plasma membrane and filamentous actin (F-actin)²³, to the cell cortex²⁴. Moe is a member of the ERM protein family that organizes specialized membrane domains by interacting with phospholipids and the cytoskeleton²⁴⁻²⁷. Moe is activated via phosphorylation that causes rigidification and rounding of the plasma membrane during mitosis²⁴. Once cells are ready to divide, Moe is dephosphorylated and detached from PIP2 at the plasma membrane, and the membrane relaxes²⁶.

Aberrant Moe signaling results in mitotic defects. For example, inhibition of Moe phosphorylation causes detachment from PIP2, disrupting membrane structure during early mitosis²⁴. Another study reports that Moe deletion results in aberrant asymmetric mitotic spindles and chromosome misalignment²⁷. Precise control of cell morphogenesis is critical for both mitosis and interphase, despite that aberrant Moe signaling is less studied among interphase cells.

Actin filaments, binding partners of Moe, are among the major components of the cytoskeleton that support cell structure²⁸. Notably, PTEN is an important regulator of actin polymerization. One study

reports cellular phagocytosis of opportunistic fungi²⁹ depends on the interaction of PTEN and cofilin-1, an actin depolymerizing factor. Loss of PTEN diphosphatase activity disrupts actin polymerization necessary for phagocytosis and cell motility²⁹.

In this study, we aim to assess how *Pten* loss impacts interphase cellular morphogenesis and cortical actin architecture using a combined qualitative and quantitative analysis of immunofluorescence images at the single-cell level. Our data revealed the absence of PTEN corresponds with cortical enrichment of F-actin, increased levels of pMoe away from the membrane, and prominent non-mitotic cell rounding. These alterations reverse when actin polymerization is blocked with an inhibitor. This may suggest that abnormal actin polymerization phenotypes in *Pten* null cells may drive aberrant cell shape and surface architecture. These results have significant implications for understanding the role of PTEN in guarding the membrane dynamics and integrity against cytoskeleton deregulation and cell cortical aberrations.

Results

Cellular morphological changes and cytoskeletal actin disorganization in the absence of *Pten*.

Throughout the years of studying PTEN and culturing adherent mammalian cells with and without *PTEN*, we have noticed a morphological feature associated with *PTEN* loss, i.e., cell rounding and detaching from culture plates or surrounding cells. To investigate and document morphological alterations following *PTEN* depletion, we traced single cell cytoskeletal architecture by immunofluorescence of F-actin using an isogenic pair of mouse embryonic fibroblast cells derived from *Pten*^{WT} and *Pten*^{KO} mice.

The cell shape is visibly rounder in cells depleted of *PTEN* (Fig. 1a). We measured the cell length and width and found decreased cell length but increased cell width in *Pten*^{KO} cells. The length-to-width (L:W) ratio in *Pten*^{KO} cells is decreased significantly (Fig. 1b). There is also a significantly higher number of round cells in *Pten*^{KO} compared to *Pten*^{WT} cells (Fig. 1c). We excluded mitotic cells that would more likely be round using the DAPI stain.

Additionally, we report higher frequency of poorly aligning actin filaments pointing in different directions in cells depleted of *PTEN*. This is contrasted with *Pten*^{WT} cells, which we found have more well-aligned F-actin bundles (Fig. 1d). Furthermore, there is more F-actin accumulated at the cell cortex in *Pten*^{KO} cells compared to *Pten*^{WT} cells (Fig. 1a and 1e). There appears to be a correlation between loss of *Pten* and enhanced enrichment of F-actin along the plasma membrane. These results suggest that PTEN is required for proper formation and distribution of actin cytoskeleton to support normal cell morphology.

Higher levels of pMoe and increased formation of pMoe aggregates in *Pten*^{KO} cells. F-actin is crosslinked to the plasma membrane through the adapter protein Moe²³. PTEN has been reported to regulate Moe during mitosis²⁴. However, the interaction between PTEN and Moe during interphase is not well studied. The crosslinking activity of Moe is dependent on its phosphorylation of a conserved threonine residue

T558 that induces a conformational change to an “active” state³⁰. We thus examined the activation status of Moe in *Pten*^{WT} and *Pten*^{KO} MEFs by focusing on pMoe levels.

The level of pMoe is significantly different between *Pten*^{WT} and *Pten*^{KO} MEFs cells (Fig. 2a). We used immunofluorescence to assess quantity of pMoe and F-actin expression. Figure 2b shows both increased F-actin membrane enrichment and increased overall pMoe levels to the naked eye in cells depleted of *Pten*. An overlay of the two targets shows visibly different morphological phenotypes in *Pten*^{KO} cells as compared to *Pten*^{WT} cells. However, we were unable to document a visible difference in Moe after *Pten* loss (Fig. 2c).

We measured the quantity of pMoe levels and found significantly higher intensity of pMoe in *Pten*^{KO} cells, which agrees with our visual assessment (Fig. 2d). In addition to higher pMoe intensity, there is a higher number of cells with prominent, compact, and punctate pattern of pMoe deposition in *Pten*^{KO} cells (Fig. 2e). We called these “aggregates,” or highly concentrated collections of pMoe which was also visually deciphered (Fig. 2b). These results support that *Pten* deletion may alter F-actin-binding protein Moe, manifested both biochemically (i.e., increased pMoe levels) and morphologically (pMoe aggregates). Thus, it is likely that Moe is a signaling target of PTEN.

Higher pMoe expression found near the nucleus as opposed to membrane in *Pten*^{KO} cells. In addition to altered activity of Moe, it is possible that *Pten* loss changes the localization of pMoe in the cell. We performed cellular fractionation experiments to measure pMoe levels in the cytoplasm and membrane (Fig. 3a). In *Pten*^{WT} cells, a non-uniform pattern of Moe and pMoe was found. More pMoe is present at the membrane. However, in *Pten*^{KO} cells, the opposite trend was found. A lower level of pMoe was found at the membrane compared to the cytoplasm. No significant difference between Moe levels near the membrane and cytoplasm was found between *Pten*^{WT} and *Pten*^{KO} cells (Fig. 3a).

We further categorized the distribution of Moe and pMoe into two specific regions: near the plasma membrane (juxtamembrane region) and near the nucleus (perinuclear region, Fig. 3b). Lower levels of pMoe in the juxtamembrane region and higher levels in the perinuclear region were found in *Pten*^{KO} cells (Fig. 3c and 3d). We further partitioned the cytoplasm to investigate the cellular distribution of pMoe and Moe in *Pten*^{KO} cells (Fig. 3e). The two areas are the peripheral area (P) and the central area (C). We found significantly higher levels of pMoe in the central area in *Pten*^{KO} cells compared to *Pten*^{WT} cells (Fig. 3f). This corresponds with an increased pMoe C:P ratio in *Pten*^{KO} cells (Fig. 3g).

Additionally, we measured the levels F-actin in the central and peripheral areas as well to determine if there might be correlation with the significant changes in pMoe localization we found between *Pten*^{KO} and *Pten*^{WT} cells. Indeed, we found a significant decrease in the F-actin C:P ratio in *Pten*^{KO} cells (Fig. 3h). In other words, more actin filaments accumulate in the peripheral area after *Pten* loss, which is in agreement with greater F-actin enrichment at the membrane (Fig. 1e). The inverse redistribution of pMoe

and F-actin suggests that their cross-linking may be hampered in the absence of *Pten*, which may lead to the impairment of cell cortical architecture.

Reversible F-actin cortical enrichment and greater cell rounding in *Pten*^{KO} cells. Given previous findings of increased actin filaments at the cortex in *Pten*^{KO} cells, we hypothesize that loss of *Pten* may affect actin polymerization. To test this hypothesis, we treated *Pten*^{KO} cells with cytochalasin D, an inhibitor of actin polymerization, to determine whether it can reverse the morphological and F-actin distribution aberrations in *Pten*^{KO} cells.

Both *Pten*^{WT} and *Pten*^{KO} cells were treated with cytochalasin D for assessment of F-actin expression at the membrane and cytoplasm. We found visible differences in both cell shape and F-actin signals after treatment between *Pten*^{KO} and *Pten*^{WT} cells (Fig. 4a). Quantitative imaging analysis shows a nearly complete reverse of F-actin membrane enrichment in *Pten*^{KO} cells treated with cytochalasin D (Fig. 4b). There is also a significant increase in the F-actin C:P ratio after cytochalasin D treatment (Fig. 4c), indicating that inhibition of actin polymerization in *Pten*^{KO} cells displaces F-actin from the membrane and that more F-actin becomes present in the cytoplasm.

Despite the correction of aberrant cortical enrichment and subcellular distribution of F-actin by inhibition of actin polymerization (Fig. 4a-4c), the organization of F-actin fibers (i.e., how well fibers aligned with each other and homogeneity of direction) remains poorly aligned in *Pten*^{KO} cells even after cytochalasin D treatment (Fig. 4d). Interestingly, there is a significantly lower number of round cells in *Pten*^{KO} treated with cytochalasin D compared to *Pten*^{KO} without treatment (Fig. 4e). These data suggest that impairment of actin filament alignment per se may not be responsible for the cell shape deregulation in *Pten*^{KO} cells.

Reversible Moe phosphorylation and subcellular localization in *Pten*^{KO} cells in response to inhibition of actin polymerization. Finally, we strived to determine if correcting aberrant actin polymerization can ameliorate the abnormal pMoe mislocalization in *Pten*^{KO} cells. We used cytochalasin D to inhibit actin polymerization and compared pMoe levels and distribution in *Pten*^{KO} and *Pten*^{WT} cells. First, we found a time-dependent reduction of pMoe in *Pten*^{KO} cells following cytochalasin D (Fig. 5a). We also found visibly decrease size and intensity of compact and punctate pMoe deposition after cytochalasin D in both *Pten*^{KO} cells (Fig. 5b). There is a significant reduction of measured pMoe levels in *Pten*^{KO} cells after cytochalasin D, which is in agreement with our visual impression (Fig. 5c).

The cellular localization of pMoe was also categorized into central (C), peripheral (P), perinuclear, and juxtamembrane. We found significantly decreased levels of pMoe in the central area (lower C:P ratio), decreased levels in the perinuclear region, and increased levels in the juxtamembrane region after cytochalasin D in *Pten*^{KO} cells (Fig. 5d-5f). Following inhibition of actin polymerization, the reversed elevation of pMoe levels and membrane dissociation of Moe (Fig. 5) co-occur with the reverse of F-actin cortical enrichment and cell rounding (Fig. 4). These data collectively suggest that Moe deregulation and

corresponding aberrant cell morphology may be associated with dysfunction of cortical actin cytoskeleton in cells lacking *Pten*.

Discussion

PTEN is a guardian of the genome^{31–33}. In addition to maintaining structural integrity of the chromosome¹² and architecture of the mitotic spindle¹⁷, PTEN has been reported to regulate multiple morphological characteristics of the cell, including cell size³⁴ and focal adhesion³⁵. Our data in this study reveal a novel PTEN function of controlling cell shape and cortical architecture. Deletion of the *Pten* gene causes marked cell rounding and cortical accumulation of F-actin. The crosslinker between F-actin and plasma membrane, Moe, becomes phosphorylated and dissociated from cortical F-actin, which is reversible by inhibition of actin polymerization. These data demonstrate the essential role of PTEN in maintaining the structural integrity and molecular composition of the cell cortex and highlight the importance of proper formation and distribution of actin filaments in such regulation.

F-actin and Moe interact to orchestrate the cell cortex, a thin actin network underlying the plasma membrane²⁸. We found higher levels of pMoe in the cytoplasm in *Pten*^{KO} cells. The fact that inhibition of actin polymerization reduces phosphorylation of Moe and rescues its aberrant subcellular distribution indicates that regulation of Moe resides downstream of actin depolymerization by PTEN. Likewise, treating *Pten* null cells with the inhibitor of actin polymerization completely reverses the phenotype of cell rounding. These results place actin filament assembly at the center of the cell shape and cortical morphology regulation by PTEN.

PTEN is a lipid phosphatase, and its canonical function is to dephosphorylate PIP3 to PIP2, which is an essential lipid for Moe binding at the plasma membrane. Moe is activated by phosphorylation to link F-actin and PIP2, while unphosphorylated Moe is dormant and localized in the cytoplasm³⁶. In the absence of *Pten*, Moe is aberrantly activated as evident by increased pMoe levels. This activated form of Moe, however, is mainly found in the cytoplasm and displaced from the plasma membrane where it normally should be. These conflicting manifestations could be the result of defective membrane trafficking in the absence of *Pten*. Previous reports suggest that PTEN regulates endocytic trafficking³⁷ and that PTEN interacts with cytoplasmic membrane structures (i.e., cytoplasmic vesicles and endosomes)^{38,39}. It is thus plausible that PTEN loss induces Moe phosphorylation and pMoe translocation from the plasma membrane to cytoplasmic membrane structures, reflective of enhanced endocytic trafficking.

We found increased levels of F-actin at the cell membrane and increased levels of pMoe in the cytoplasm in *Pten*^{KO} cells. Whereas F-actin and pMoe are normally associated at the membrane to regulate the cell cortex, we found they were likely spatially separated in *Pten*^{KO} cells. Proper localization of F-actin and pMoe is important for their interaction. It may be inferred that PTEN loss may disrupt localization of these proteins, impacting cell morphology.

It is uncertain if defects of PTEN's lipid phosphatase function may be directly responsible for the increased F-actin levels at the membrane. It is, however, possible that increased F-actin at the membrane in the absence of PTEN may increase roundness and stiffness of cells. The interplay of PTEN and actin may be important for cell morphology. Based on these observations and hypotheses, we further explored the potential interaction between PTEN and actin by using cytochalasin D, which inhibits actin polymerization. We found decreased F-actin levels at the membrane and increased levels in the cytoplasm in *Pten*^{KO} cells. We also found fewer round cells after inducing actin depolymerization. It seems that actin depolymerization reversed the phenotypic changes caused by loss of PTEN (i.e., actin depolymerization corresponded with lower F-actin levels at the membrane and fewer round cells). It remains uncertain if the activity of actin in *Pten*^{KO} cells are a compensatory reaction to disruption in homeostasis or aberrant presentation of uncontrolled cell proliferation/migration.

Methods

Cells, antibodies and reagents. Mouse embryonic fibroblasts (MEFs) derived from *Pten* wild type (*Pten*^{WT}) and *Pten* knock-out (*Pten*^{KO}) mice have been reported on previously^{13,17} and were cultured in MEM (Gibco) supplemented with 10% fetal bovine serum. The primary antibodies used were: PTEN (A2B1, sc-7974) and actin (I-19, sc-1616) from Santa Cruz, and Moesin (ab151542) and p-Moesin (ab177943) from Abcam. The Phalloidin-iFluor™ 488 conjugate (#20549) and cytochalasin-D (#11330) were from the Cayman Chemical Company.

Protein extraction, fractionation, and Western blotting. Cells harvested and suspended in PBS containing protease inhibitors were subjected to sonication using multiple on and off cycles in a Qsonica Q500 sonicator to obtain total cell lysates. For cellular fractionation, 10% of the harvested cells were aliquoted for whole cell lysates. The remaining cells were centrifuged and resuspended with a hypotonic lysis buffer (HLB) containing Digitonin and protease inhibitors for the cytoplasmic fraction (10mM Tris, pH 7.5, 10mM NaCl, 3mM MgCl₂, 10% glycerol, H₂O, 50ug/mL Digitonin), and subsequently with HLB containing IGEPAL and protease inhibitors for the membrane fraction (10mM Tris, pH 7.5, 10mM NaCl, 3mM MgCl₂, 10% glycerol, H₂O, 0.3% IGEPAL-C630). Protein samples were subjected to standard a Western blotting protocol to determine the levels of Pten, Moe, and pMoe. Briefly, protein samples were loaded in a 10% polyacrylamide gel for electrophoresis and subsequently transferred to a PVDF membrane. Targeted proteins were probed by specific primary antibodies followed by HRP-conjugated secondary antibodies for signal development using ECL reagents (Pierce PI32209).

Immunofluorescence microscopy. Cells were cultured on glass slides overnight, fixed in 4% paraformaldehyde diluted in PBS for 15 min, then underwent permeabilization with 0.1% Triton X-100 for 10 min. Cells were washed carefully with PBS, followed by incubation with a blocking solution (1% BSA in PBS and 0.1% tween20) and a 0.1% Triton X-100 solution for membrane permeabilization. The cells were stained with a primary antibody (pMoe or Moe) for 2 hours at room temperature, and then with a fluorochrome-conjugated secondary antibody for 1 hour at 37°C in a dark incubator. Stained cells were

imaged using a Nikon Eclipse TiE microscope. Phalloidin was used for F-actin staining, following the manufacturer's protocol. Images were acquired at 20- and 40-times magnifications and as z-stacks with 0.2 to 0.4 μm spacing to generate maximum-intensity projection of the entire cell. Imaging data were analyzed with NIS-Elements AR 4.11, Fiji, and ImageJ software.

Qualitative imaging analysis. We categorized the shape of cells using F-actin as the approximate membrane marker. Cells that appeared circular, not spreading out, and contoured were classified as "round." All other cells were listed as "not round." Then, we studied Moe and pMoe expression by classifying the size, density, and distribution of foci. "Aggregates" were discrete or aggregated signals of Moe or pMoe. Diffuse signals that appeared scattered were "not aggregates". Lastly, F-actin activity was also studied. We focused on the distribution of the F-actin signal (i.e., close to membrane or in cytoplasm). We F-actin filaments and assess whether they are aligning or not aligning.

Quantitative imaging analysis. Stained cells acquired from immunofluorescence were first analyzed for their cellular and nuclear area, lengths, and widths. The areas of the cell and nuclei were measured in μm^2 with the loop function in Fiji/ImageJ using the mono (DIC) and blue-fluorescent (DAPI) channels, respectively. The line segment function was used to measure the width and length of cells in μm^{40} . The fluorescence intensity levels of Moe, pMoe, and F-actin were measured using Fiji/ImageJ⁴¹. Given the measured area of the selected cell, the mean fluorescence of background readings, and its integrated density, the corrected total cell fluorescence (CTCF) is calculated. CTCF is a measure of the fluorescence intensity that accounts for subtracting out the background signal. An additional corrected mean cell fluorescence (CMCF) was calculated by dividing CTCF with the cellular area to determine the fluorescence intensity per μm^2 . Only CMCF data are shown in this paper. At least three different background readings were measured to calibrate the CTCF calculation. Statistical tests were performed to identify data significance. The localized intensity of Moe, pMoe, and F-actin near the nucleus ("perinuclear") and (membrane "juxtamembrane") were also distinguished using the loop function in Fiji/ImageJ. Our research approximated the near-nucleus region by finding the midpoint of the cytoplasmic region between the plasma membrane and the nuclear membrane. The near-nucleus region quantified the Moe, pMoe, and F-actin intensity within the mid-area closer to the nucleus that is stained blue (DAPI). The intensity near the membrane was quantified using the area closer to the plasma membrane. Statistical tests were also applied to these data.

Statistical analysis. The collected quantitative data were analyzed by either unpaired t test (when group number = 2) or one way ANOVA followed by Tukey's multiple comparisons test (when group number > 2). For qualitative data analysis, raw data were first converted to a frequency distribution table, then subjected to unpaired t test or one-way ANOVA followed by Sidak's multiple comparison test. The statistical significances between data sets were expressed as p values, where ns means not significant, * for $p < 0.05$, ** for $p < 0.01$, *** for $p < 0.001$, and **** for $p < 0.0001$.

Declarations

Author Contributions

W.H.S. conceived the study and designed the experiments. S.S.P. performed most experiments and captured immunofluorescence images. K.H., S.S.P., and W.H.S. created the multilevel factorial design for imaging analysis. K.H., E.S., A.C., G.H.L., and W.H.S. conducted data and statistical analysis. M.L. and X.F. performed experiments for preliminary studies. X.F. provided supervision on imaging data analysis. K.H., S.S.P., E.R.N., and W.H.S. wrote the manuscript. All the authors discussed the results and proofread the manuscript. K.H. and S.S.P. contributed equally to this work.

Data Availability Statement

All relevant data are available from the corresponding author (W.H.S.) upon request and/or are included with the manuscript.

Acknowledgements

This study was supported by NIH grant R01GM100478, Irma T. Hirschl/Monique Weill-Caulier Trust, and Alice Bohmfalk Charitable Trust.

Conflict of Interest

The authors declare no conflict of interest.

References

1. Li, J. *et al.* PTEN, a putative protein tyrosine phosphatase gene mutated in human brain, breast, and prostate cancer. *Science* **275**, 1943-1947, doi:10.1126/science.275.5308.1943 (1997).
2. Teng, D. H. *et al.* MMAC1/PTEN mutations in primary tumor specimens and tumor cell lines. *Cancer Res* **57**, 5221-5225 (1997).
3. Maehama, T. & Dixon, J. E. The tumor suppressor, PTEN/MMAC1, dephosphorylates the lipid second messenger, phosphatidylinositol 3,4,5-trisphosphate. *J Biol Chem* **273**, 13375-13378, doi:10.1074/jbc.273.22.13375 (1998).
4. Garcia-Cao, I. *et al.* Systemic elevation of PTEN induces a tumor-suppressive metabolic state. *Cell* **149**, 49-62, doi:10.1016/j.cell.2012.02.030 (2012).
5. Liu, J. & Feng, Z. PTEN, energy metabolism and tumor suppression. *Acta Biochim Biophys Sin (Shanghai)* **44**, 629-631, doi:10.1093/abbs/gms048 (2012).
6. Ramaswamy, S. *et al.* Regulation of G1 progression by the PTEN tumor suppressor protein is linked to inhibition of the phosphatidylinositol 3-kinase/Akt pathway. *Proc Natl Acad Sci U S A* **96**, 2110-2115, doi:10.1073/pnas.96.5.2110 (1999).
7. Brandmaier, A., Hou, S. Q. & Shen, W. H. Cell Cycle Control by PTEN. *J Mol Biol* **429**, 2265-2277, doi:10.1016/j.jmb.2017.06.004 (2017).

8. Liliental, J. *et al.* Genetic deletion of the Pten tumor suppressor gene promotes cell motility by activation of Rac1 and Cdc42 GTPases. *Curr Biol* **10**, 401-404, doi:10.1016/s0960-9822(00)00417-6 (2000).
9. Lacalle, R. A. *et al.* PTEN regulates motility but not directionality during leukocyte chemotaxis. *J Cell Sci* **117**, 6207-6215, doi:10.1242/jcs.01545 (2004).
10. Groszer, M. *et al.* PTEN negatively regulates neural stem cell self-renewal by modulating G0-G1 cell cycle entry. *Proc Natl Acad Sci U S A* **103**, 111-116, doi:10.1073/pnas.0509939103 (2006).
11. Yilmaz, O. H. *et al.* Pten dependence distinguishes haematopoietic stem cells from leukaemia-initiating cells. *Nature* **441**, 475-482, doi:10.1038/nature04703 (2006).
12. Shen, W. H. *et al.* Essential role for nuclear PTEN in maintaining chromosomal integrity. *Cell* **128**, 157-170, doi:10.1016/j.cell.2006.11.042 (2007).
13. Sun, Z. *et al.* PTEN C-terminal deletion causes genomic instability and tumor development. *Cell Rep* **6**, 844-854, doi:10.1016/j.celrep.2014.01.030 (2014).
14. He, J., Kang, X., Yin, Y., Chao, K. S. & Shen, W. H. PTEN regulates DNA replication progression and stalled fork recovery. *Nat Commun* **6**, 7620, doi:10.1038/ncomms8620 (2015).
15. Bassi, C. *et al.* Nuclear PTEN controls DNA repair and sensitivity to genotoxic stress. *Science* **341**, 395-399, doi:10.1126/science.1236188 (2013).
16. Kang, X. *et al.* PTEN stabilizes TOP2A and regulates the DNA decatenation. *Sci Rep* **5**, 17873, doi:10.1038/srep17873 (2015).
17. He, J. *et al.* PTEN regulates EG5 to control spindle architecture and chromosome congression during mitosis. *Nat Commun* **7**, 12355, doi:10.1038/ncomms12355 (2016).
18. van Ree, J. H., Nam, H. J., Jeganathan, K. B., Kanakkanthara, A. & van Deursen, J. M. Pten regulates spindle pole movement through Dlg1-mediated recruitment of Eg5 to centrosomes. *Nat Cell Biol* **18**, 814-821, doi:10.1038/ncb3369 (2016).
19. Zhang, Z. *et al.* PTEN regulates PLK1 and controls chromosomal stability during cell division. *Cell Cycle* **15**, 2476-2485, doi:10.1080/15384101.2016.1203493 (2016).
20. Chen, Z. H. *et al.* PTEN interacts with histone H1 and controls chromatin condensation. *Cell Rep* **8**, 2003-2014, doi:10.1016/j.celrep.2014.08.008 (2014).
21. Gong, L. *et al.* Nuclear PTEN tumor-suppressor functions through maintaining heterochromatin structure. *Cell Cycle* **14**, 2323-2332, doi:10.1080/15384101.2015.1044174 (2015).
22. Javadi, A. *et al.* PTEN controls glandular morphogenesis through a juxtamembrane beta-Arrestin1/ARHGAP21 scaffolding complex. *Elife* **6**, doi:10.7554/eLife.24578 (2017).
23. Solinet, S. *et al.* The actin-binding ERM protein Moesin binds to and stabilizes microtubules at the cell cortex. *J Cell Biol* **202**, 251-260, doi:10.1083/jcb.201304052 (2013).
24. Roubinet, C. *et al.* Molecular networks linked by Moesin drive remodeling of the cell cortex during mitosis. *J Cell Biol* **195**, 99-112, doi:10.1083/jcb.201106048 (2011).

25. Carreno, S. *et al.* Moesin and its activating kinase Slik are required for cortical stability and microtubule organization in mitotic cells. *J Cell Biol* **180**, 739-746, doi:10.1083/jcb.200709161 (2008).
26. Kunda, P. *et al.* PP1-mediated moesin dephosphorylation couples polar relaxation to mitotic exit. *Curr Biol* **22**, 231-236, doi:10.1016/j.cub.2011.12.016 (2012).
27. Kunda, P., Pelling, A. E., Liu, T. & Baum, B. Moesin controls cortical rigidity, cell rounding, and spindle morphogenesis during mitosis. *Curr Biol* **18**, 91-101, doi:10.1016/j.cub.2007.12.051 (2008).
28. Chugh, P. *et al.* Actin cortex architecture regulates cell surface tension. *Nat Cell Biol* **19**, 689-697, doi:10.1038/ncb3525 (2017).
29. Serezani, C. H. *et al.* PTEN directly activates the actin depolymerization factor cofilin-1 during PGE₂-mediated inhibition of phagocytosis of fungi. *Sci Signal* **5**, ra12, doi:10.1126/scisignal.2002448 (2012).
30. Matsui, T. *et al.* Rho-kinase phosphorylates COOH-terminal threonines of ezrin/radixin/moesin (ERM) proteins and regulates their head-to-tail association. *J Cell Biol* **140**, 647-657, doi:10.1083/jcb.140.3.647 (1998).
31. Kritikou, E. PTEN – a new guardian of the genome. *Nature Reviews Molecular Cell Biology* **8**, 179-179, doi:10.1038/nrm2128 (2007).
32. Hou, S. Q., Ouyang, M., Brandmaier, A., Hao, H. & Shen, W. H. PTEN in the maintenance of genome integrity: From DNA replication to chromosome segregation. *Bioessays* **39**, doi:10.1002/bies.201700082 (2017).
33. Fan, X., Kraynak, J., Knisely, J. P. S., Formenti, S. C. & Shen, W. H. PTEN as a Guardian of the Genome: Pathways and Targets. *Cold Spring Harb Perspect Med* **10**, doi:10.1101/cshperspect.a036194 (2020).
34. Kim, J. S. *et al.* Mechanistic analysis of a DNA damage-induced, PTEN-dependent size checkpoint in human cells. *Mol Cell Biol* **31**, 2756-2771, doi:10.1128/MCB.01323-10 (2011).
35. Tamura, M. *et al.* Inhibition of cell migration, spreading, and focal adhesions by tumor suppressor PTEN. *Science* **280**, 1614-1617, doi:10.1126/science.280.5369.1614 (1998).
36. Fehon, R. G., McClatchey, A. I. & Bretscher, A. Organizing the cell cortex: the role of ERM proteins. *Nat Rev Mol Cell Biol* **11**, 276-287, doi:10.1038/nrm2866 (2010).
37. Shinde, S. R. & Maddika, S. PTEN modulates EGFR late endocytic trafficking and degradation by dephosphorylating Rab7. *Nat Commun* **7**, 10689, doi:10.1038/ncomms10689 (2016).
38. Leslie, N. R. & Downes, C. P. PTEN function: how normal cells control it and tumour cells lose it. *Biochem J* **382**, 1-11, doi:10.1042/BJ20040825 (2004).
39. Vazquez, F. *et al.* Tumor suppressor PTEN acts through dynamic interaction with the plasma membrane. *Proc Natl Acad Sci U S A* **103**, 3633-3638, doi:10.1073/pnas.0510570103 (2006).
40. Lepekhn, E. A., Walmod, P. S., Berezin, A., Berezin, V. & Bock, E. Evaluation of cell morphology. *Methods Mol Biol* **161**, 85-100, doi:10.1385/1-59259-051-9:085 (2001).

Figures

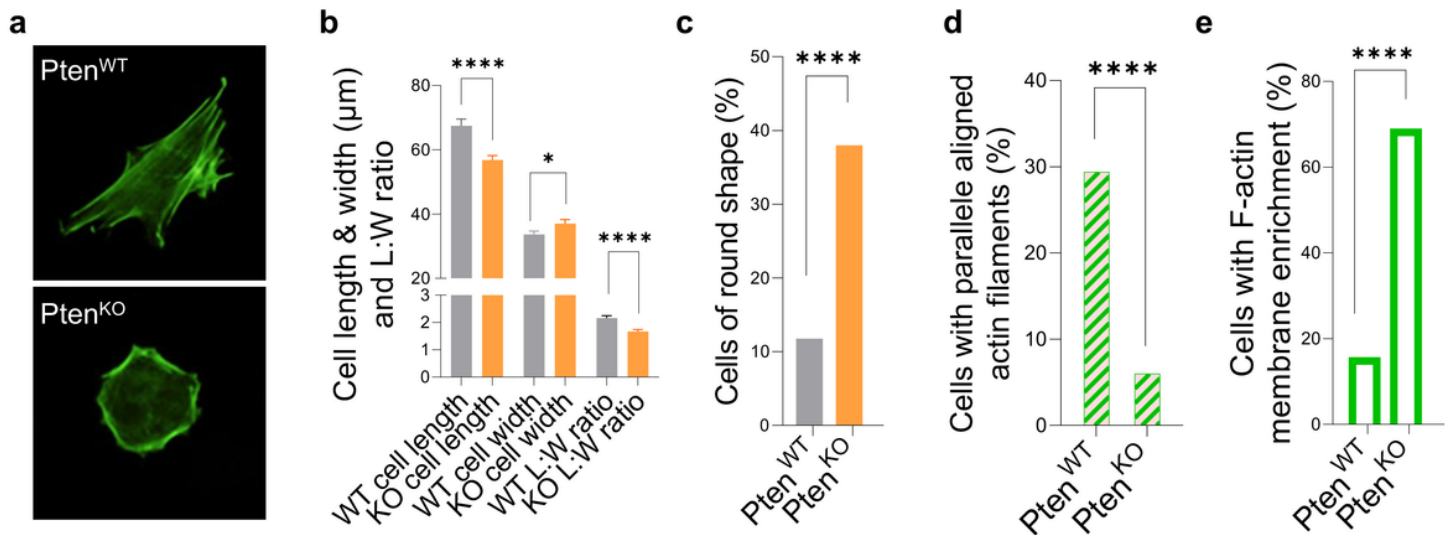


Figure 1

Pten knockout (*Pten*^{KO}) cells correlate with morphological changes and cytoskeleton disorganization. Mouse embryonic fibroblast cells (MEFs) derived from *Pten*^{WT} and *Pten*^{KO} mice were labeled by phalloidin and subjected to fluorescent microscopy examination of actin filaments. **a**. Representative fluorescence images of *Pten*^{WT} and *Pten*^{KO} MEFs labeled with phalloidin. **b**. Cell length and width were measured (n≥100), and the ratio of length:width (L:W) was calculated for each cell and summarized in the histogram. **c**. Cell shape is categorized into “round” and “not round” and presented as the percentage of round cells. **d**. Cells are categorized into “having” or “not having” well organized (prominent and aligning) actin cytoskeletal fibers”. The percentage of cells with well-organized fibers were assessed. **e**. The percentage of cells with F-actin enriched at the cell membrane were reported.

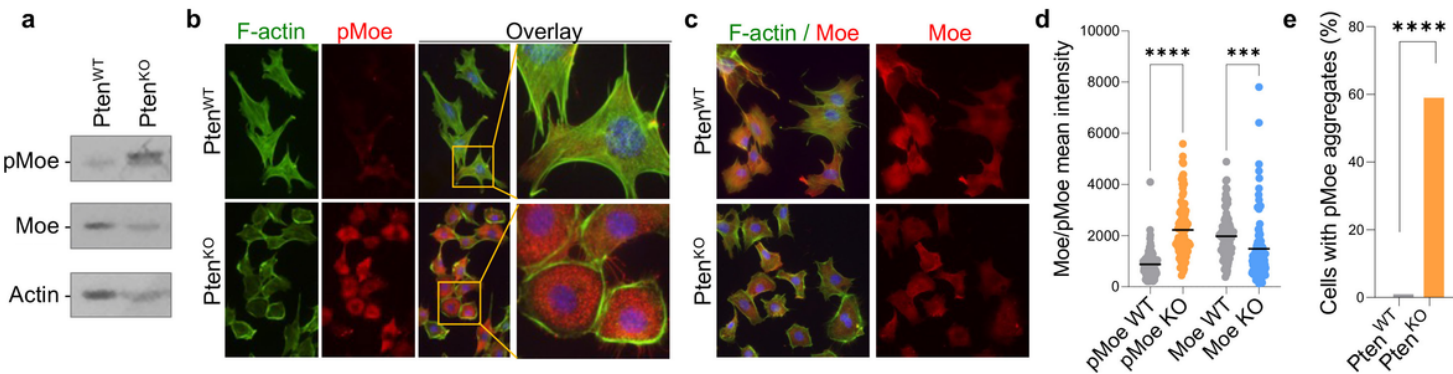


Figure 2

Higher levels of pMoe with an imaging manifestation of increased pMoe aggregates in *Pten*^{KO} cells. a. Western blotting of *Pten*^{WT} and *Pten*^{KO} MEFs depicting levels of pMoe, Moe and actin. **b.** Representative fluorescence images of *Pten*^{WT} and *Pten*^{KO} MEFs, showing pMoe and F-actin signals individually and overlayed. Selected regions are magnified for visual enhancement. **c.** Representative fluorescence images of Moe and F-actin co-staining. **d.** Mean intensity of Moe and pMoe in *Pten*^{WT} and *Pten*^{KO} MEFs (n≥100 for each line) were measured and summarized in the scatterplot. The percentage of cells with pMoe aggregates are presented. Aggregates are concentrated and punctate signals of pMoe, as illustrated in 1b.

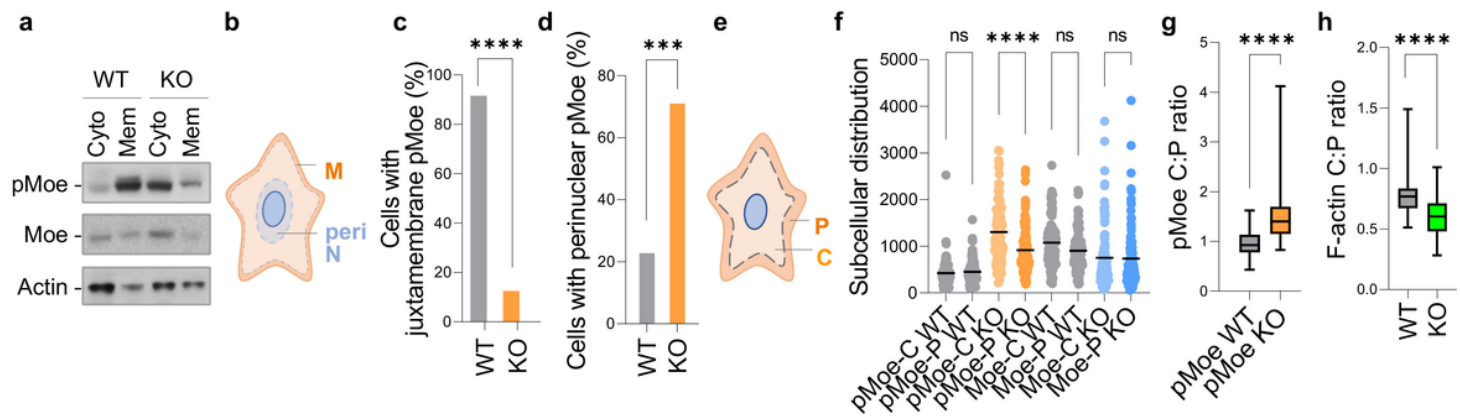


Figure 3

Greater subcellular dislocation of pMoe towards the cytoplasm and perinuclear region in *Pten*^{KO} cells. a. Western blotting of *Pten*^{WT} and *Pten*^{KO} MEFs following a cellular fractionation procedure, depicting the expression levels of pMoe, Moe, and actin in the cytoplasmic and membrane fractions. **b.** Schematic indicating the boundaries used to assess regions near the nuclear membrane (periN) or plasma membrane (M). **c.** pMoe localization is characterized based on vicinity to the membrane, or “juxtamembrane” if next to the cell membrane. The percentage of cells with juxtamembrane accumulation of pMoe is presented. **d.** pMoe localization is characterized based on vicinity to the nucleus, or “perinuclear” if close to the nuclear membrane. The percentage of cells with perinuclear accumulation of pMoe is reported. **e.** Schematic indicating the boundaries used to assess peripheral/membrane (P) and central/cytoplasmic (C) regions. **f.** The distribution of Moe and pMoe in the peripheral and central areas was quantified (n≥100 for each cell line). **g.** The ratio of central to peripheral (C:P) pMoe levels was calculated for each cell and summarized in the histogram. **h.** The ratio of F-actin present in the cytoplasm and membrane are reported as a C:P ratio.

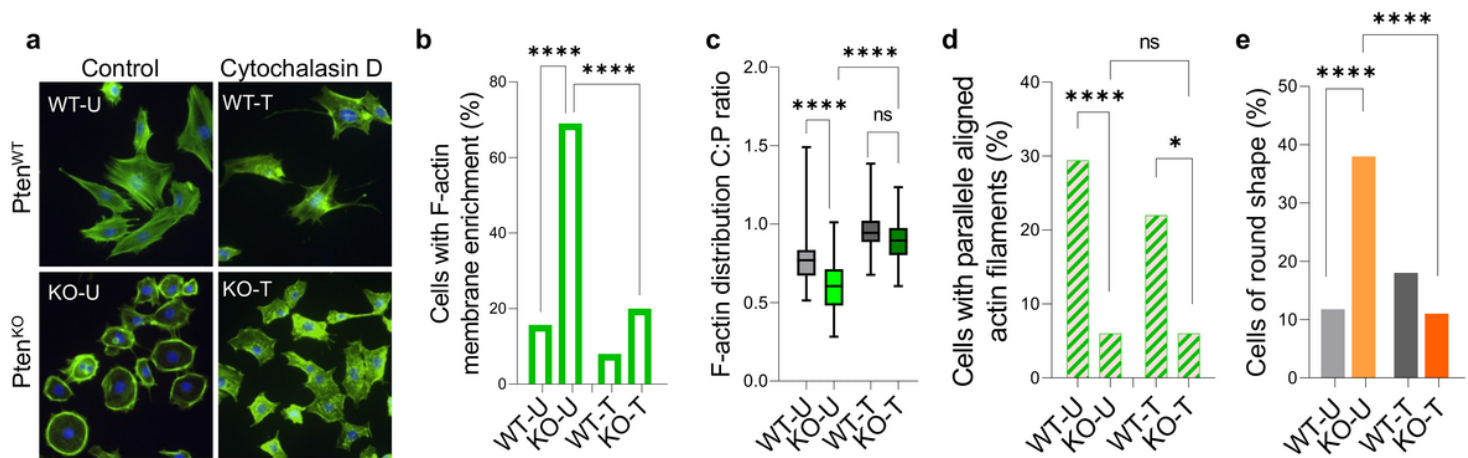


Figure 4

Inhibition of F-actin polymerization decreases membrane enrichment and reduces cell rounding in *Pten*^{KO} cells. **a.** Representative fluorescence images of *Pten*^{WT} and *Pten*^{KO} MEFs labeled with phalloidin before (U) and after (T) cytochalasin D treatment (200nM, 4h). **b.** The percentage of cells with F-actin enriched at the cell membrane before and after cytochalasin D treatment is reported. **c.** The ratio of F-actin presented in the cytoplasm and membrane before and after cytochalasin D treatment are reported as a C:P ratio. **d.** The percentage of cells with prominent and aligning actin fibers before and after cytochalasin D treatment was assessed. **e.** Cell shape is categorized into “round” and “not round” and presented as the percentage of round cells.

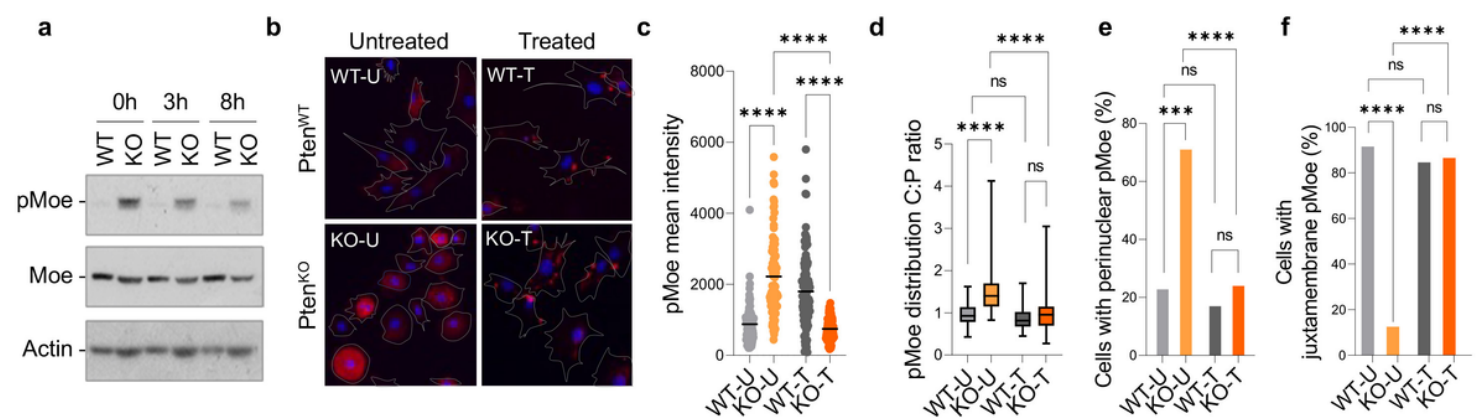


Figure 5

F-actin depolymerization correlates with decreased pMoe levels and altered pMoe localization in *Pten*^{KO} cells. **a.** Western blotting of *Pten*^{WT} and *Pten*^{KO} MEFs following cytochalasin D treatment for different time periods as indicated, depicting the expression levels of pMoe, Moe, and actin. **b.** Representative fluorescence images of pMoe (red) in *Pten*^{WT} and *Pten*^{KO} MEFs before (U) and after (T) cytochalasin D

treatment (200nM, 4h). Nuclei were stained by DAPI and cells were outlined by dotted lines. **c.** Mean intensity of pMoe signals was quantified before and after cytochalasin D treatment ($n \geq 100$ for each condition). **d.** The ratio of central to peripheral (C:P) was calculated for each cell and summarized in the histogram. **e.** pMoe localization is characterized based on vicinity to the membrane. The percentage of cells with juxtamembrane accumulation of pMoe before and after cytochalasin D treatment is reported. **f.** pMoe localization is characterized based on vicinity to the nucleus. The percentage of cells with perinuclear accumulation of pMoe before and after cytochalasin D treatment is presented.

Supplementary Files

This is a list of supplementary files associated with this preprint. Click to download.

- [SRSupplementaryInformation.pdf](#)